Journal of Membrane Science 579 (2019) 162–171

Contents lists available at ScienceDirect

Journal of Membrane Science

journal homepage: www.elsevier.com/locate/memsci

# Biofouling-resistant nanocellulose layer in hierarchical polymeric membranes: Synthesis, characterization and performance

Pejman Hadi[a,b,c], Mengying Yang[a,c], Hongyang Ma[a], Xiangyu Huang[a,c], Harold Walker[d,*], Benjamin S. Hsiao[a,c,**]

[a] Department of Chemistry, Stony Brook University, Stony Brook, NY, 11794, USA
[b] Department of Civil Engineering, Stony Brook University, Stony Brook, NY, 11794, USA
[c] New York State Center for Clean Water Technology, Stony Brook University, Stony Brook, NY, 11794, USA
[d] Department of Civil and Environmental Engineering, Worcester Polytechnic Institute, Worcester, MA, 01609, USA

ARTICLE INFO

*Keywords:*
Membrane fouling
Ultrafiltration
Nanocellulose
Super-hydrophilic
Electrostatic repulsion

ABSTRACT

In this study, we developed a hierarchical thin-film nanofibrous composite (TFNC) membrane with electrospun mat as substrate and hydrophilic nanocellulose as the antifouling barrier layer. We found that, due to the super-hydrophilic nature of the nanocellulose, the contact angle of the barrier layer (20 – 28°) decreased rapidly with time and reached nearly zero after a few seconds, whereby the membrane flux were remarkably higher (52 $L.\ m^{-2}.\ h^{-1}$) than conventional polymeric membranes (4 – 14 $L.\ m^{-2}.\ h^{-1}$) at a very low transmembrane pressure of 0.5 psi. In addition, the membrane surface was considerably more negatively-charged due to the high concentration of carboxylate groups, resulting in higher repulsive electrostatic forces between the barrier layer and the model foulant. As a result, the nanocellulose-based hierarchical membranes exhibited a lower fouling tendency (<10%) and a higher degree of protein rejection ratio compared with the conventional membranes (fouling tendency >30%). The effect of the nanocellulose layer thickness on the membrane fouling was also examined and it was demonstrated that the nanocellulose barrier layer thickness had a significant effect on the membrane fouling. The higher flux, lower fouling, and good rejection properties of this membrane system suggest nanocellulose is a promising barrier material for filtration membranes for water purification and other separation processes.

## 1. Introduction

Membrane technologies are at the core of many water purification applications due to their versatility and high separation efficiencies [1,2]. However, many membrane processes still remain energy intensive despite continued advances in membrane materials [3]. Furthermore, performance reduction due to fouling remains quite common and a major impediment in a number of applications [4]. Fouling results in the narrowing or clogging of the membrane pores through the deposition and accumulation of organic, inorganic, or biological molecules/particles on the membrane surface [5–7]. This phenomenon leads to the reduction in permeate flux at a constant applied pressure, or the increase in transmembrane pressure (TMP) where a constant permeate flow rate is desired [6]. According to Jiang et al., biofouling is one of the most common causes of fouling [8]. Therefore, development of biofoulant-resisting membranes has received increasing attention.

In order to reduce the biofouling, several strategies have been examined. Shon et al. found that ferric chloride flocculation followed by activated carbon adsorption was an attractive method to remove 90% of the total organic carbon (TOC) [9]. Introduction of slow-releasing biocides, such as encapsulated silver nanoparticles to prevent the growth of microorganisms is another technique that was explored [10]. However, all these methods require the introduction of a secondary process or a chemical, which can be costly and may result in secondary contamination. One of the most common and practical techniques for the preparation of biofoulant-resisting membranes is membrane modification. Membrane modification refers to either membrane polymer modification through copolymerization [11], blending [12], or grafting [13] with a more functional hydrophilic polymer (pre-treatment), introduction of a hydrophilic additive into the membrane polymer [14], or surface-modification of the polymer, for example using plasma [15] or electron irradiation [16] (post-treatment). All these treatment

* Corresponding author. Department of Civil and Environmental Engineering, Worcester Polytechnic Institute, Worcester, MA, 01609, USA.
** Corresponding author. Department of Chemistry, Stony Brook University, Stony Brook, NY, 11794, USA.
*E-mail addresses:* hwwalker@wpi.edu (H. Walker), benjamin.hsiao@stonybrook.edu (B.S. Hsiao).

https://doi.org/10.1016/j.memsci.2019.02.059
Received 4 January 2019; Received in revised form 21 February 2019; Accepted 22 February 2019
Available online 27 February 2019
0376-7388/ 

methods aim to increase the hydrophilicity of the membranes, as it is widely acknowledged that more hydrophilic surfaces are less prone for biofouling.

Although hydrophilicizing the membrane surface by these methods is very attractive and useful in reducing membrane fouling, there are some limitations with these techniques. For example, Ravereau et al. pointed out that additive-free membranes exhibited no significant change in performance by ageing (through several steps of chemical washing), whereas the hydrophilicity of the membranes with hydrophilic additives were completely removed by ageing [17]. Also, the blending of hydrophilic and hydrophobic polymers is feasible, but the modified membranes only render limited hydrophilicity.

Cellulose nanofibers (CNFs), on the other hand, exhibit super-hydrophilic properties due to the abundance of hydroxyl and carboxyl functional surface groups [18–21], however, the strong *van der Waal* forces and inter- and intramolecular hydrogen bonds within the fibers maintain their insolubility in water. Therefore, due to its hydrophilicity and negatively-charged surface functional moieties, the use of functionalized CNF for fabrication of low fouling, high-flux hierarchical membranes for water purification has great potential in a range of practical applications.

There have been several promising studies on the application of CNF as a barrier layer in membranes. For example, Visanko et al. used a vacuum filtration method for the preparation of CNF-based membranes and tested their flux and fouling [22,23]. We postulate that if the porosity of the substrate is increased, the flux can be further increased and the membrane can have higher performance. Therefore, in this study, a highly porous (> 80%) nanofibrous scaffold prepared by the electrospinning technique was used as a substrate in order to maximize flux and reduce energy consumption in membrane operations. However, these electrospun membranes remain susceptible to fouling [24]. This fouling is likely due to the high porosity of the scaffold, as well as any possible attraction forces between the foulant particles and electrospun nanofibers if they still contain residual opposite electric charges. To alleviate the fouling issue, we coated a layer of CNF, as the barrier layer, on the electrospun substrate to reduce the interaction between the charged substrate and the foulant molecules/particles and thus, reducing fouling. The CNF barrier layer adopted an interwoven structure due to the high aspect ratio of the nanocellulose fibers. Our group has already pioneered the development of high flux CNF-coated electrospun ultrafiltration membranes for oil/water emulsion separation [25–27]. However, the biofouling properties of these membranes and the effect of CNF-coating thickness on their anti-biofouling properties have yet to be studied.

Jiang et al. developed a biofouling-resistant ultrafiltration membrane, which was a nanocellulose-graphene oxide composite [8]. Although the antifouling property of the membrane was very promising, the fabrication of the composite membrane was a challenging process. Also, the superior properties of the CNF (hydrophilicity and functional moieties) was used to offset the unfavorable properties of the graphene oxide (high fouling). Because a lot of the CNF functional groups may be masked by the matrix when used within a composite, our hypothesis was to coat – rather than blend in composite form – a thin layer of pure CNF on top of the porous polymer matrix, so that the CNF layer acts as an antifouling superhydrophilic thin film on the membrane. Therefore, in this study, we investigated the fouling behavior of thin-film nanofibrous composite (TFNC) membranes containing a hierarchical structure with nonwoven poly(etheyelene terephtalate) (PET) substrate, porous electrospun polyacrylonitrile (PAN) mid-layer support, and hydrophilic CNF barrier layer of different thicknesses. The performance of these TFNC membranes was compared with commercial polymer-based membranes, prepared by the phase inversion method, with similar pore size. Detailed characterization of the CNF layer, the effects of surface charge and layer thickness, were correlated with the fouling tendency using bovine serum albumin (BSA) protein as a model biofoulant. In addition to examining the biofouling-resistant properties of the CNF layer, this study also aims at investigating the effect of CNF layer thickness on the antifouling properties of hierarchical membrane.

## 2. Experimental

### 2.1. Materials

Commercial-grade ultrafiltration (UF) membranes, PVDF-A6 (MWCO 500 kDa), PVDF-V6 (MWCO 500 kDa), PAN-PX (MWCO 400 kDa), and PES-LX (MWCO 300 kDa), were purchased from the Sterlitech Corporation. Chemical agents: 2,2,6,6-Tetramethyl-1-piperidinyloxy (TEMPO, 98%), sodium bromide (NaBr), sodium hypochlorite (NaOCl, 14.5% available chlorine) and bovine serum albumin (BSA, fraction V, 97%) were purchased from the Fisher Scientific and used as received. Softwood pulp, made predominately from Loblolly Pine, was supplied by the International Paper Company. The received pulp was already delignified by oxygen delignification, followed by the chlorine dioxide process to remove the remaining lignin.

### 2.2. Preparation of cellulose nanofibers

Cellulose nanofibers were extracted from wood pulp via TEMPO-mediated oxidation method according to previously published literature [25]. Briefly, 10.0 g delignified wood pulp was dispersed in 500.0 g of deionized water. Sodium bromide (1.0 g) and TEMPO agent (0.2 g) were subsequently added into the dispersion and mixed well to reach homogeneity. The pH level of the suspension was adjusted to and maintained at a value of 10.0 ± 0.2 throughout the reaction process by addition of 1 M NaOH solution. The oxidation reaction was initiated by adding 112.0 g NaOCl under continuous stirring for 24 h. The pH change was rapid at the initial stages of the experiment, suggesting that the reaction was very fast, but it became less noticeable after a few hours. The reaction was stopped by adding 50 ml ethanol solution and stirring for 30 min. The final product was separated by centrifugation at ~6000 rpm. Then, the resultant product was washed and centrifuged again. Finally, the product was placed in a dialysis bag until the conductivity of the medium was $<5\,\mu S/cm$. The concentration of the bulk cellulose nanofiber (CNF) suspension was measured to be 0.3 wt%.

### 2.3. Preparation of hierarchical TFNC membranes

A 12 $^{w}/_{w}\%$ homogenous PAN solution was first prepared by dissolving PAN (M.W. 150,000 g/mol) in DMF at 60 °C overnight. PAN nanofibers were subsequently electrospun on a PET nonwoven substrate under a voltage of 18 kV and at a flowrate of 10 $^{\mu l}/_{min}$. The distance between the spinneret and the rotating metal drum (i.e., the collector, having a diameter of 9 cm and a rotating speed of 300 rpm) was fixed at 12.5 cm. The thickness of the electrospun PAN nanofiber layer was fixed in the range of $80-100\,\mu m$. The resulting electrospun scaffold was first soaked in an HCl acid solution ($pH = 2$) for 30 min until all its pores were filled with the acidic solution. Then, the electrospun scaffold was laid on a flat glass plate, where excessive acidic solution was removed by rolling using a glass rod. Subsequently, three different concentrations of cellulose nanofiber (CNF) suspensions were applied to the top of the electrospun scaffold to fabricate different thicknesses of CNF barrier layer. Since the CNF suspension became a gel upon contact with the acidic environment, it did not penetrate into the pores of the supporting PAN layer. In these TFNC membranes, $E-CNF1$ and $E-CNF3$ were used to represent the membranes with thickest and thinnest CNF layers, respectively. Finally, all TFNC membranes were heat-treated at 110 °C for 20 min before testing.

### 2.4. Membrane characterization

The surface and cross-sectional morphologies of the TFNC membranes were characterized by a focused ion beam-scanning electron

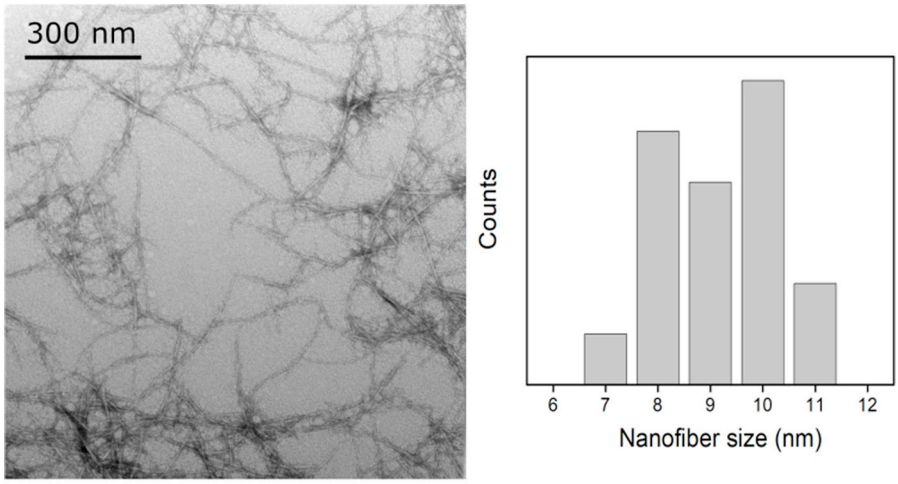


**Fig. 1.** TEM image of the cellulose nanofibers obtained by TEMPO-mediated oxidation technique and their fiber size distribution.

microscope (FIB-SEM, crossbeam 340; Carl Zeiss Microscopy, LLC). The membrane samples were first mounted on the SEM stubs with carbon tape and then were sputter-coated in high vacuum with Au/Pd using a Leica EM ACE600. A 30 kV 300 pA FIB probe was used to mill the surface to achieve $10 \times 5\,\mu m\,(W \times D)$ cross-section and 3 kV of EHT was applied to examine the morphology. The individual cellulose nanofiber images were obtained using a FEI BioTwinG2 transmission electron microscope (TEM) equipped with an AMT XR-60 CCD digital camera system at an accelerating voltage of 120 kV. In the sample preparation for TEM, a 10 µL droplet of cellulose nanofiber solution was deposited on a carbon-coated TEM grid (Ted Pella Inc.) and the excess liquid was absorbed by a piece of clean filter paper. Then, a small drop of 2.0% uranyl acetate negative stain was added. The uranyl acetate excess solution was subsequently removed, allowing the blotted piece to dry on the grid.

The surface functional groups of the CNF barrier layer, before and after the protein filtration, were evaluated by Fourier transform infrared (FTIR, PerkinElmer Spectrum One) spectroscopy equipped with the attenuated total reflection (ATR) configuration. The spectra with a resolution of $4\ cm^{-1}$ and 64 scans per spectrum were recorded in the transmittance mode between the wavenumber range of $4000 - 400\ cm^{-1}$. The dynamic water contact angle of the barrier layer was determined by a Dataphysics (OCA 15 EC) Contact Angle Analyzer. In this test, a glass syringe with an inner diameter of 0.52 mm was used to obtain 4 µl droplets with a dosing rate of $2\ {}^{\mu l}/_{s}$. An Electrokinetic Analyzer (Anton Paar, SurPASS 3) was also used to measure the streaming potential of the CNF barrier layer. In this test, the membrane samples were mounted on an adjustable gap cell ($20\ mm \times 10\ mm$) with a gap distance of about $110 - 120\ \mu m$. Finally, a pH titration was performed on the membrane from the initial pH of 3.5 to the final pH value of 8.5 using a 1 mM KCl as the electrolyte solution.

### 2.5. Evaluation of the protein filtration performance

A clear-cast acrylic Sterlitech crossflow membrane cell with an active membrane area of $42\ cm^2$ was used to evaluate the pure water flux and bovine serum albumin (BSA) fouling behavior of the TFNC and conventional membranes. The filtration test was carried out at a flow rate of 0.8 gpm and a transmembrane pressure of 0.5 psi. A heat exchanger was used to avoid any increase in the temperature of the retentate solution as a result of the pump shear. An ultraviolet/visible spectrophotometer (UV/Vis, Thermo Scientific Genesys™ 10S) with a high intensity xenon lamp was used to measure the BSA absorbance (and hence the concentration using the calibration curve) in a desired solution at a wavelength of 278 nm. The membrane permeation flux ($J$) was measured according to the following equation:

$$J = {}^{V}/_{(A \times t)} \tag{1}$$

where $V$ is the volume of the permeate flowing through the membrane at a certain amount of time ($t$), and $A$ is the effective membrane area. The rejection of the BSA by the membranes ($R_t$) was determined by measuring the BSA concentration in the bulk solution ($C_0$) and in the permeate ($C_t$) as follows:

$$R_t = \left(1 - \frac{C_t}{C_0}\right) \times 100 \tag{2}$$

## 3. Results and discussion

### 3.1. Properties of cellulose nanofibers

Arvidsson et al. carried out a life cycle assessment of CNF preparation by mechanical treatment and two different chemical treatments and concluded that the mechanical treatment required a lot of energy and was an obstacle for CNF production [28]. Therefore, in this study, TEMPO-mediated oxidation was adopted to prepare the CNF. The TEMPO-mediated oxidation method is an effective way to defibrillate the cellulose microfiber bundles into nanofibers [29–31]. This method relies on the regioselective conversion of primary hydroxyl groups on to carboxylate moieties, rendering negative charges on the cellulose surface under the aqueous environment. The electrostatic repulsive forces greatly facilitate the defibrillation process. Fig. 1 illustrates the TEM image of CNF extracted from the delignified wood pulp using the TEMPO oxidation method. These CNFs exhibited an average width of $7 - 11\ nm$, which generally agreed with previously-reported CNF widths [32,33]. We believe these fibers have a ribbon shape, probably with a thickness in the range of $2 - 3\ nm$, as examined by small-angle neutron scattering (SANS) and small-angle x-ray scattering (SAXS) techniques [34]. We note that the change of the biomass species as well as the oxidation conditions can greatly affect the resulting fiber cross-sectional dimensions and length. For example, Isogai et al. demonstrated that when the oxidation conditions were more severe, the charge density of CNF were high leading to a smaller cross-sectional size in the range of $3 - 4\ nm$ due to a greater extent of defibrillation. In our chosen oxidation conditions, the resulting carboxylate content on the CNF was found to be 1.2 mmol/g, which was moderately high. Previous studies have reported that C6 aldehyde groups can also be formed during the TEMPO-oxidation reaction, as an intermediate structure before the complete oxidation to carboxylate groups, or as depolymerization linkages as a result of β-elimination in the cellulose structure [35]. The presence of aldehyde groups on the CNF is quite

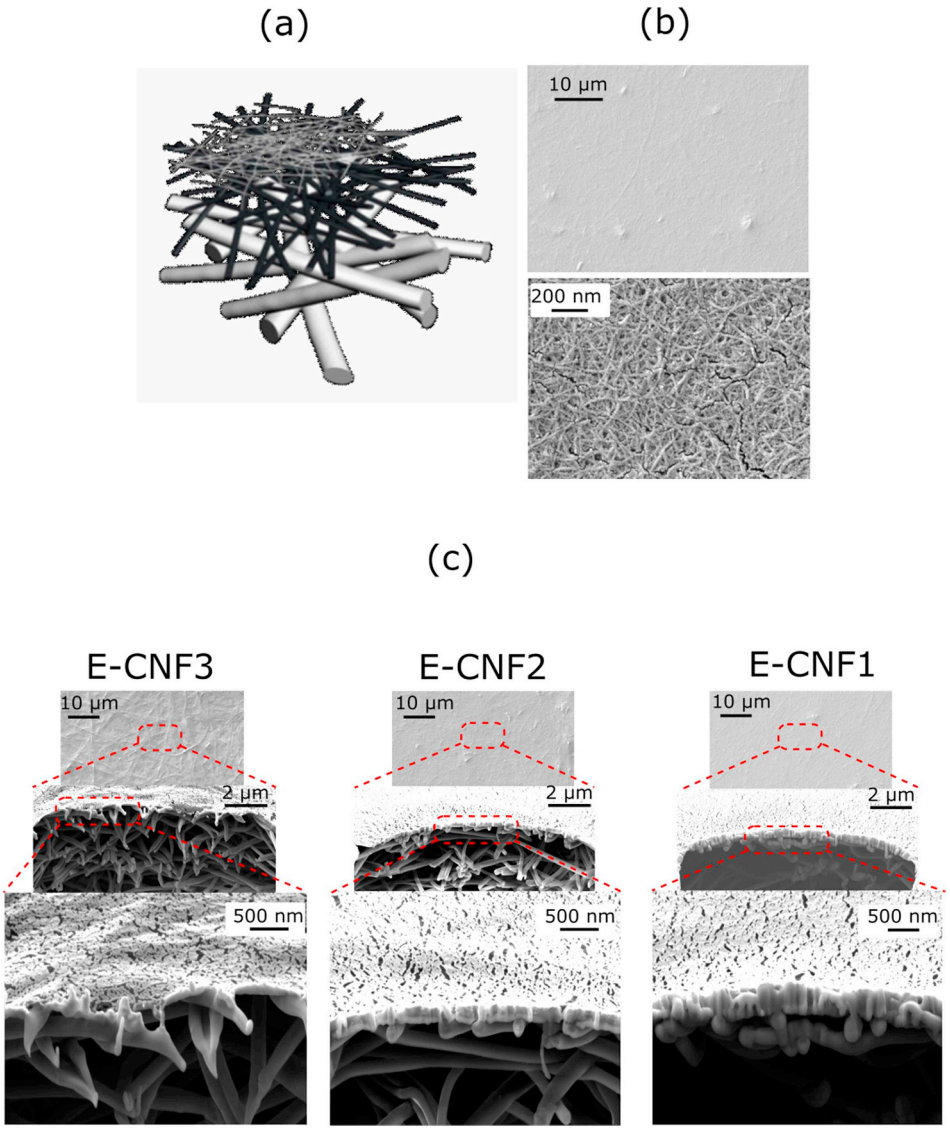


**Fig. 2.** (a) Schematic representation of the hierarchical structure of the typical CNF-based TFNC membrane. (b) SEM image of the top CNF barrier layer of $E-CNF2$ membrane at different magnifications (the cracks are resulted from the high energy beam damage at higher magnifications). (c) Cross-sectional SEM images of the $E-CNF1$, $E-CNF2$, and $E-CNF3$ at different magnifications.

desirable in membrane fabrication, since the aldehyde groups can react with hydroxyls and form hemiacetals to partially crosslink the nanofibers and impart stability under heat. However, higher aldehyde content may suggest a high degree of depolymerization [36], i.e. shorter nanofiber lengths, which is undesirable.

### 3.2. Morphology of the hierarchical membranes

A schematic illustration of the hierarchical structure of the demonstrated TFNC membrane is shown in Fig. 2a. In this structure, the nonwoven PET substrate (with a fiber diameter about 20 $\mu m$ and the pore size of over 5 $\mu m$) provides the mechanical strength and structural stability. The mid-layer consists of electrospun polyacrylonitrile (PAN) nanofibers scaffold, with a mean pore size of $\sim 0.4-0.6\,\mu m$ and has very high porosity ($\sim$80%). The high porosity of the electrospun scaffold is partially resulted from the high electrostatic repulsion between the charged nanofibers. The third layer is an ultrathin CNF barrier layer, responsible for the filtration of the contaminants (e.g. BSA proteins here). The thickness of this barrier layer has been varied in this study to examine the effect of the layer thickness on the flux and antifouling properties. In comparison to the PAN nanofibers in the electrospun mat, CNF is more hydrophilic – later evidenced by the contact angle measurements – and provides a much smaller surface texture. The non-woven feature of CNF in the barrier layer creates interconnected pores with size about a few times larger than the fiber cross-sectional dimensions, where these pores can pass water molecules while retaining undesirable molecules/particles with diameters larger than the pores. Since the CNF cross-sectional dimension is in the range of 7–11 nm, the demonstrated TFNC membranes are suitable for UF applications.

The surface images of a typical CNF-coated TFNC membrane observed by SEM at different magnifications are shown in Fig. 2b. As CNF can be easily damaged by radiation, it was not feasible to obtain a very high quality image of the CNF surface at very high magnification. The cracks observed in these images at higher magnifications were caused by the high energy electron beam as the original TFNC membrane was free of any defects. Based on these images, the average pore size of the CNF barrier layer is in the range of $30-40\ nm$.

Fig. 2c illustrates both surface and cross-sectional views of SEM images of three CNF-coated TFNC membranes with different thicknesses (i.e., $E-CNF1$, $E-CNF2$ and $E-CNF3$). Among these membranes, $E-CNF1$ possessed the largest thickness and $E-CNF3$

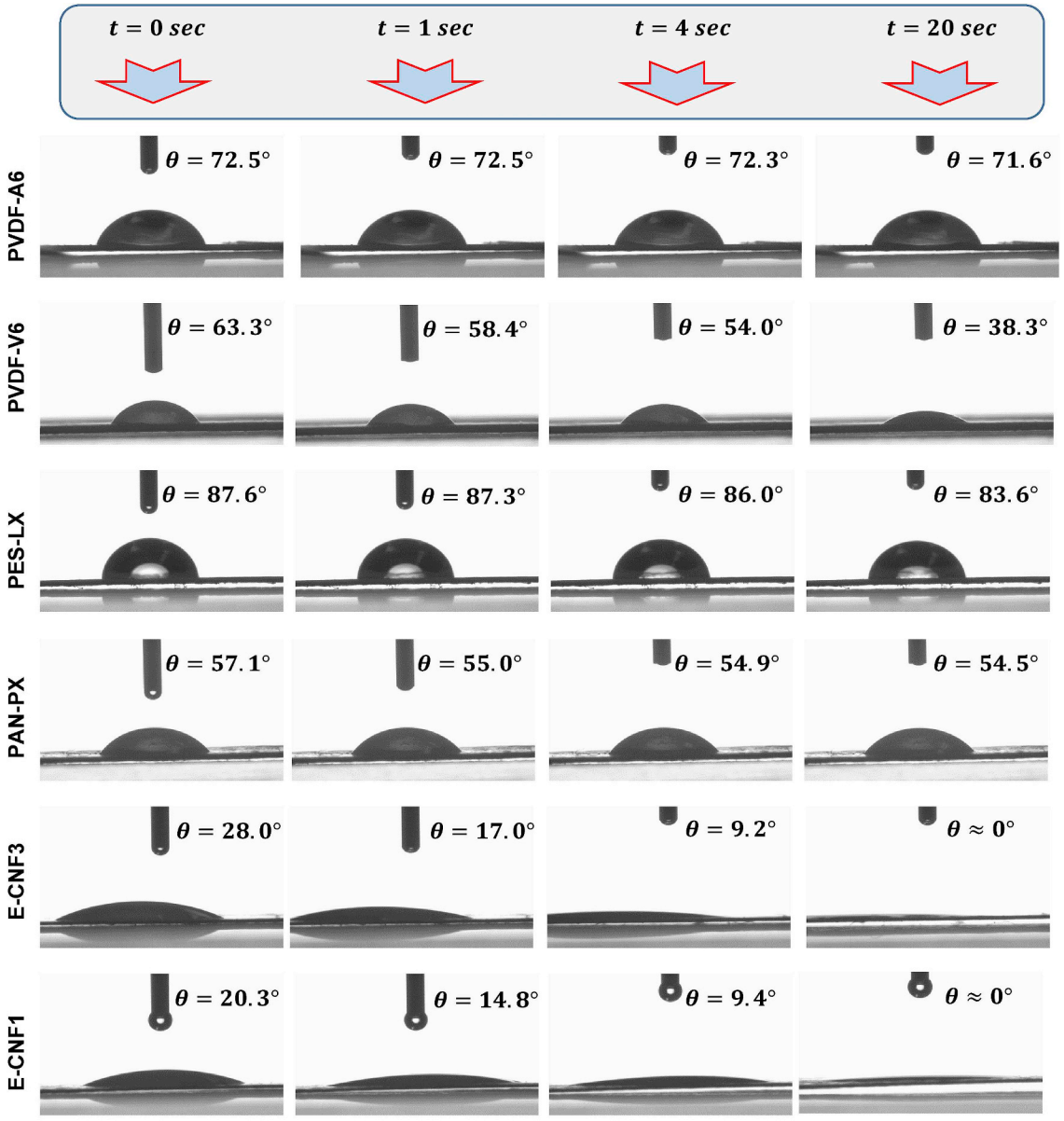


**Fig. 3.** Dynamic contact angle (CA) measurements of the conventional polymeric membranes and novel CNF-based TFNC membranes.

possessed the smallest thickness. It was found that $E-CNF3$ had the most uneven topography, where the barrier layer surface reflected the structure of supporting electrospun nanofibers underneath. As the barrier layer thickness increased, a much flatter topography appeared. The thickness of the CNF barrier layer was quantitatively measured using a Focused Ion Beam (FIB) technique to examine the cross-section of the membrane. As depicted in Fig. 2c, the CNF barrier layer thickness of the $E-CNF3$, $E-CNF2$, and $E-CNF1$ were determined ~108 nm, ~210 nm, and ~264 nm, respectively. The trend of increasing CNF layer thickness coincided well with the applied CNF concentration.

### 3.3. Surface characterization of the CNF barrier layer

As discussed earlier, the surface of the CNF has abundant functional groups with high affinity for water molecules, making them especially suitable as hydrophilic barrier layer materials. Fig. 3 depicts the dynamic water contact angles of $E-CNF1$, $E-CNF3$ and several conventional polymer-based UF membranes, having similar average pore sizes as the CNF-based TFNC membranes. Most of these conventional polymeric membranes have hydrophobic surfaces and they are prone to the fouling problems due to the hydrophobic aggregation with amphiphilic foulants, such as proteins, polysaccharides, and bacteria [37]. The reduction of the surface hydrophobicity usually can improve the fouling tendency [37–39]. In this test, the contact angles for $PVDF-A6$, $PVDF-V6$, $PES-LX$ and $PAN-PX$ were found to be 72.5°, 63.3°, 87.6°, and 57.1°, respectively. The contact angles of these membranes exhibited a very slight change over time (Fig. 3). In contrast, the dynamic contact angles of the $E-CNF1$ and $E-CNF3$ membrane were very different from the conventional polymeric membranes. $E-CNF1$, for example, had a contact angle of 20.3° upon the initial contact, which was much lower than all the conventional polymeric membranes. After 1 $s$ and 4$s$, the contact angle decreased to 14.8° and 9.4°, respectively. After 20$s$ (or less), the water droplet was totally absorbed into the membrane matrix. These results suggest that immediately after the contact between the water droplet and the membrane surface, it is attracted to the functional group-rich CNF layer and absorbed within the pores created by the cellulose nanofibers. The very rapid decrease in the contact angles of the TFNC membrane may also partially contribute to the very high water flux. It was found that the

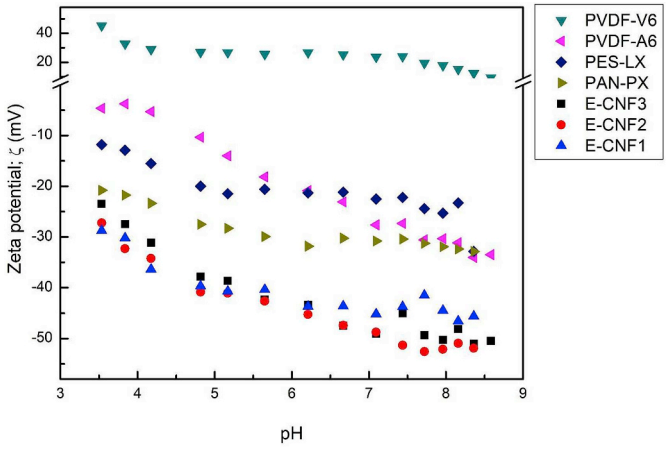


**Fig. 4.** Zeta potential values of the TFNC and conventional UF membranes at various pH values and a fixed ionic strength (1 mM KCl).

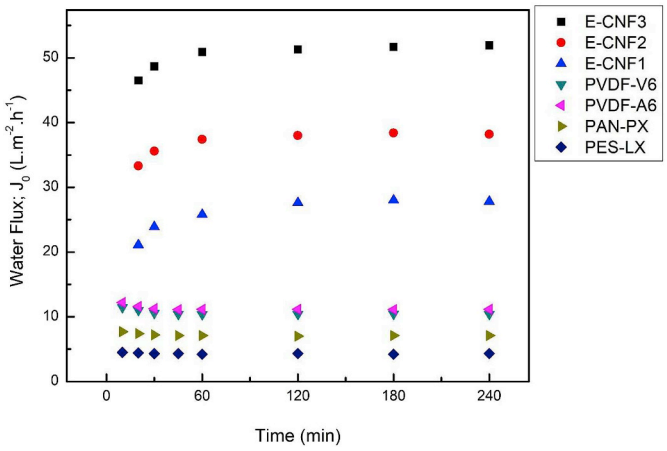


**Fig. 5.** Pure water flux measurements for TFNC and conventional UF membranes.

changes in the contact angle for the conventional polymeric membranes were very minimal, even though these membranes have been rendered to be "hydrophilic". Perhaps, this is because the applied chemical treatment only introduced limited concentration of functional groups to the predominant nonpolar hydrophobic matrix. As a result, there was not sufficient driving force to attract water molecules into the polymer matrix, where the contact angle exhibited a minimal change. Although the contact angle is acknowledged as an important criterion to affect the fouling tendency of the membrane, we believe that the notable difference in the "contact angle change rate" between the CNF-based TFNC membranes and conventional polymeric membranes implies a large difference in their membrane structure and the permeation flux under the fixed transmembrane pressure (TMP).

Fig. 4 illustrates the zeta potential values of the TFNC membrane and conventional polymer membrane surfaces at different pH values but under a fixed ionic strength (1 mM KCl). It was seen that all three CNF-based TFNC membranes, irrespective of the CNF layer thickness, exhibited more negatively-charged surfaces compared with the conventional polymeric membranes. This is expected as the CNF layer has abundant carboxylate functional groups ($COO^{-}$) formed by the TEMPO-mediated oxidation reaction, where CNFs are negatively-charged at all pH values. The three TFNC membranes, with different CNF thicknesses, exhibited similar zeta potential values and an increasing trend (more negative) with the increasing pH value. It was found that the CNF membranes exhibited a zeta potential of $\sim -45\ mV$ at a pH of 6.5, while the zeta potentials of the conventional polymeric membranes ranged from $-20 \sim -30\ mV$ at the same pH value.

### 3.4. Membrane filtration performance

The pure water flux values of the three different TFNC membranes and conventional polymeric membranes under similar operating conditions are shown in Fig. 5. It was found that in conventional polymer-based membranes, the pure water flux decreased slightly with time until it reached a plateau value, which was probably due to the membrane compression at the applied pressure. However, this trend was reversed for all three TFNC membranes, where the water flux increased noticeably with time. Such an increase could be attributed to the swelling of the CNF barrier layer by water molecules. In other words, the swelling behavior probably made the average pore size larger, allowing water molecules to pass through the layer easier. It was found that the flux increase reached a plateau value after 2 h of continuous operation. Under the steady-state conditions, the flux values of TFNC membranes, irrespective of the CNF layer thickness, were remarkably higher than those of conventional polymer-based membranes. For example, the pure water flux values for $PAN-PX$, $PES-LX$, $PVDF-A6$ and $PVDF-V6$ were $7.1\ L.m^{-2}.h^{-1}$, $4.3\ L.m^{-2}.h^{-1}$, $11.1\ L.m^{-2}.h^{-1}$ and $13.0\ L.m^{-2}.h^{-1}$, respectively at the steady state, where those for $E-CNF1$, $E-CNF2$ and $E-CNF3$ membranes were $27.8\ L.m^{-2}.h^{-1}$, $38.2\ L.m^{-2}.h^{-1}$, and $51.9\ L.m^{-2}.h^{-1}$. The significantly higher flux of the CNF based TFNC membranes compared to the conventional polymer-based membranes could be attributed to the exceptionally high porosity of the electrospun supporting layer as well as the greater hydrophilicity (thus wettability) of the CNF barrier layer. The data in Fig. 5 also indicated that the thickness of the CNF layer significantly affects the pure water flux. As the thickness of the barrier layer decreased ($264\ nm$ for $E-CNF1$; $210\ nm$ for $E-CNF2$; and $108\ nm$ for $E-CNF3$), the resistance towards the applied pressure by the membrane was reduced, and consequently, the pure water flux was increased.

It is also interesting to compare the flux of these TFNC membranes with other hierarchical membranes containing CNF. Visanko et al. found that the flux of their membranes coated with CNF via vacuum filtration were around 100 LMH at 1 bar (~14.5 psi) and they observed a linear relationship between the pressure increase and the flux enhancement [23]. The flux of our membranes with similar hierarchical structure, but different membrane development method, was found to be ~50 LMH at only 0.5 psi. Also, Mautner et al. developed wood-derived nanocellulose papers and used them as ultrafiltration membranes [40]. The flux of the best performing membrane was ~20 $LMH.MPa^{-1}$ (or 0.07 LMH at 0.5 psi). Based on these comparisons, the flux of the TFNC membranes obtained in our study show great promise for further exploration of these hierarchical membrane materials.

Fig. 6 illustrates the fouling ratio ($J/Jo$, where $J$ represents the current flux value and $Jo$ represents the initial flux value) of CNF-based TFNC and conventional polymer-based membranes at various BSA (model biofoulant) concentrations. It was seen that both $E-CNF1$ and $E-CNF2$ membranes exhibited small fouling tendency (the flux decrease was less than 10% even at the highest BSA concentration of $200\ mg.L^{-1}$). This result could be attributed to the very negative zeta potential of the CNF barrier layer surface. In other words, the strong repulsive interaction between the membrane surface (Fig. 4, it was negatively-charged at the neutral pH value) and BSA proteins (the zeta potential of BSA particle was $-20.6 \pm 1.5\ mV$ [41] and the BSA isoelectric point at pH = 4.7 [42]) resulted in lower fouling tendency. Xiao et al. elucidated the importance of surface charge and hydrophilicity on the fouling behavior of polymeric membranes and found that there was a strong relationship between the zeta potential values of the membranes and their fouling behavior [43]. In the $E-CNF3$ membrane, a notable fouling ratio was observed (the flux decrease was about 22% after $2\ hr$ of operation at a BSA concentration of $200\ mg.L^{-1}$). In Fig. 4, the zeta potential of $E-CNF3$ was similar to

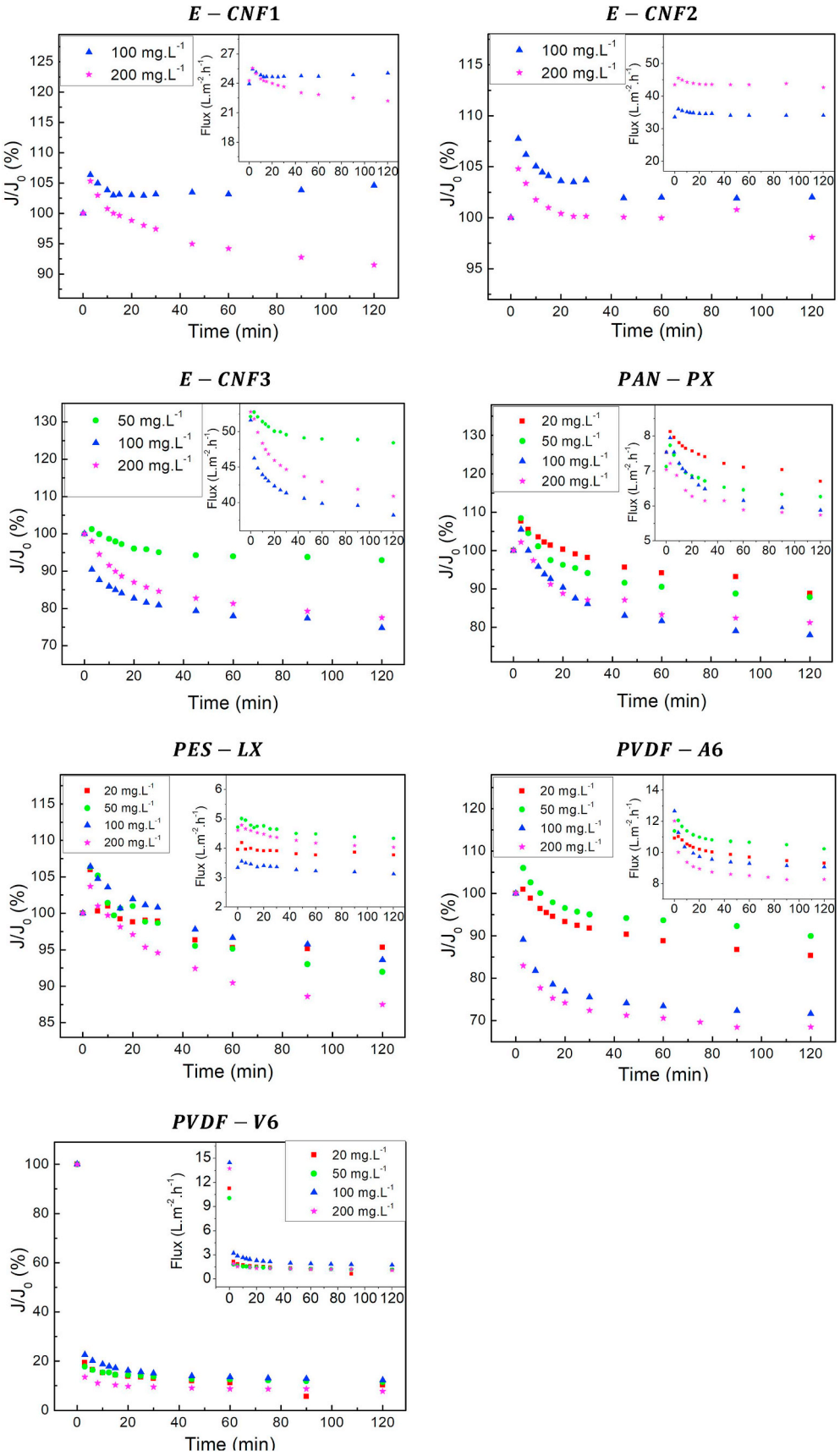


**Fig. 6.** The fouling behavior of TFNC and conventional UF membranes at various BSA protein concentrations.

that of $E-CNF2$ ($-47mV$) and slightly more negative than that of $E-CNF1$ ($-43\ mV$) at pH = 7.0. This indicates that the zeta potential alone, although a good indicator, cannot fully explain the differences in the antifouling behavior of the CNF-coated TFNC membranes.

The higher fouling ratio of $E-CNF3$ than those of $E-CNF1$ and $E-CNF2$ could be explained by the higher roughness of the former surface [44,45]. With the high surface roughness, the foulants can be more easily on the membrane surface, blocking the pores and ultimately resulting in the reduction of permeation flux. It should be noted that although $E-CNF3$ rendered a higher fouling ratio as compared with $E-CNF1$ and $E-CNF2$, its flux was still much higher than the latter two membranes as a result of the thinner barrier layer. In other words, despite the fouling, $E-CNF3$ maintained the highest flux value among all the membranes during the filtration (inset of Fig. 6).

The various conventional polymer-based membranes, on the other hand, exhibited different fouling behaviors. In specific, $PVDF-V6$ with a zeta potential of $+24\ mV$ at a pH value of 6.5 showed the highest fouling tendency. Even at BSA protein concentrations as low as $20\ mg.\ L^{-1}$, this membrane exhibited a fouling ratio of 90%. This is likely due to the strong electrostatic interactions between the positively charged $PVDF-V6$ surface and the negatively charged protein. Wang and Tang pointed out the significance of electrostatic interaction between the membrane surface and the foulant particles [46]. Among the other three conventional membranes, the fouling tendency was as follows: $PVDF-A6 > PAN-PX > PES-LX$. This generally agreed with the notion that the higher negative zeta potential led to lower fouling tendency [46] (except for $PES-LX$, which exhibited a lower negative zeta potential at pH = 7.0 among the three). It is interesting to note that the same trend was seen in the pure water flux values: $PVDF-A6$ ($\sim 11\ L.\ m^{-2}.\ h^{-1}$) > $PAN-PX$ ($\sim 7\ L.\ m^{-2}.\ h^{-1}$) > $PES-LX$ ($\sim 4\ L.\ m^{-2}.\ h^{-1}$). This suggests that in conventional polymeric membranes, as long as the surface characteristics (i.e., the contact angle and zeta potential) of the membranes are similar, their fouling tendency mainly depends on the flux property, where higher flux through the membrane will lead to higher membrane fouling. The strong dependence of membrane fouling on membrane pore size, elucidated by Xiao et al. [47], also corroborates our findings.

The FTIR spectra of pristine and BSA-fouled $E-CNF1$ and $E-CNF3$ membranes are shown in Fig. 7. In this figure, the strong broad band at $3340\ cm^{-1}$ corresponds to the stretching modes of the $O-H$ bonds. The peaks at $1606\ cm^{-1}$ are characteristic of the sodium carboxylate groups ($COO^{-}\ Na^{+}$) and free carboxyl groups ($-COOH$) [48]. All these surface moieties persisted after the protein filtration, suggesting the lack of any surface interactions between the CNF layer and the protein. In contrast, all the stretching vibrations assigned to the hydroxyl functional groups of the polymer-based membranes were absent after filtration. This observation indicates that BSA could interact with the polar groups on the conventional membrane surface, where there was no electrostatic repulsion between the membrane surface and the protein foulant. These results suggest that for long-term membrane operation (on the order of weeks or months), the lack of electrostatic repulsion may manifest itself as gradual fouling on the conventional membranes, while the CNF-based TFNC membranes can retain the electrostatic charge repulsion for longer periods of operation and thus reduce the fouling tendency.

Fig. 8 illustrates the long-term BSA protein filtration results, which confirm the superior performance properties (i.e., higher flux, higher rejection ratio and lower fouling tendency) of the nanocellulose-based TFNC membranes over the conventional UF membranes in an extended period of time. In the flux diagram of Fig. 8, the $E-CNF1$ membrane exhibited several-times higher flux values than the three chosen membranes (e.g. about 2.5X higher than $PVDA-A6$; about 4X higher than $PAN-PX$; about 7X higher than $PES-LX$). The $E-CNF1$ membrane also exhibited the lowest fouling tendency among all the membranes tested. It was seen that the major fouling for $E-CNF1$ ($\sim 7\%$) occurred in the first $2\ hr$. After the initial flux decrease, no noticeable flux change could be observed up to $48\ hr$ for $E-CNF1$, whereas the conventional polymeric membranes showed lower flux values as well as higher fouling tendency. The latter observations were in good agreement with the FTIR results, where the polar groups of the conventional polymeric membranes all disappeared during the early stages of filtration. This was in contrast with the observation that the hydroxyl groups in the CNF-based TFNC membranes remained unchanged after the BSA filtration. These results indicate that conventional polymeric membranes will gradually foul over longer periods of operation, while CNF-based TFNC membranes can stay more resistance to the long-term fouling problem while maintaining higher flux and higher rejection ratio simultaneously. Furthermore, the protein rejection ratio of the $E-CNF1$ membrane was found to be higher than the conventional polymer-based membranes. This behavior could be attributed to the stronger electrostatic repulsion between the CNF and BSA molecules (both are negatively charged) in addition to the size exclusion effect. In conventional polymer-based membranes, the electrostatic repulsion between the polymer surface and BSA molecules was probably quite weak, where the rejection ratio was mainly dominated by the size exclusion.

## 4. Conclusions

In this study, we investigated the biofouling property of a hierarchical thin-film nanofibrous composite (TFNC) membrane system, where the TEMPO-oxidized cellulose nanofibers (CNFs) were used as a

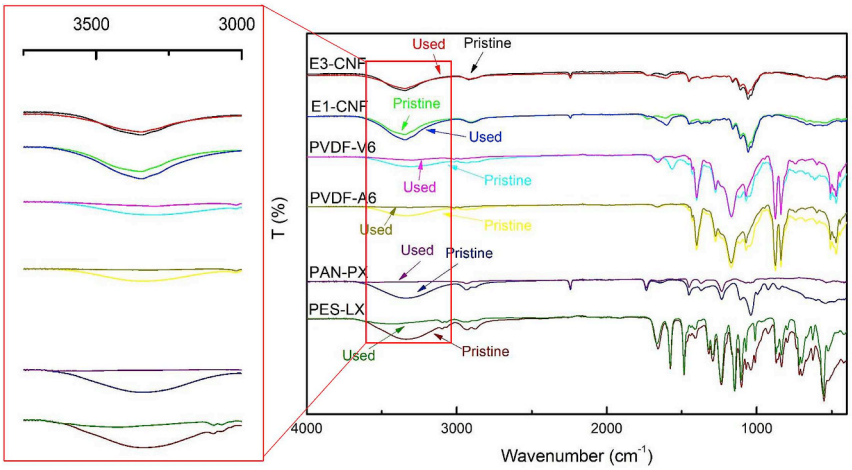


**Fig. 7.** The FTIR spectra of the conventional and CNF-based TFNC membranes before and after BSA protein filtration.

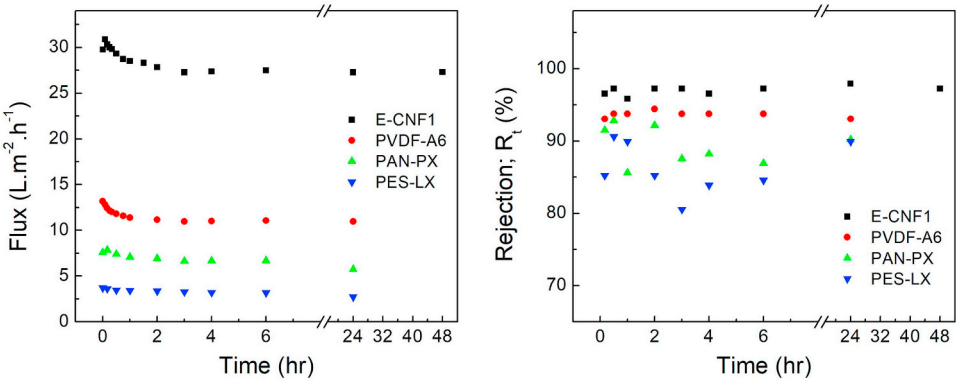


**Fig. 8.** Long term flux decay (fouling) and protein rejection ratio for TFNC and conventional membranes at a BSA concentration of 200$mg.\ L^{-1}$ .

barrier layer supported by a porous electrospun nanofibrous scaffold. The CNF barrier layer consisted of randomly deposited nanofibers, rendering an effective pore sizes around ~30 − 40 $nm$, where the nanofibers were negatively charged. The permeability of the TFNC membrane system (the pure water flux of the best performing membrane was around 52 $L.\ m^{-2}.\ h^{-1}$) was found to be superior to the conventional polymeric membranes (the pure water flux was in the range of 4 − 14 $L.\ m^{-2}.\ h^{-1}$) made by the phase inversion method. The high permeability could be attributed to the combined effect of the high porosity in the electrospun support layer (> 80%) and the hydrophilic nature of the cellulose nanofibers (the starting contact angles of the CNF barrier layer was in the range of 20 − 30°, which rapidly decreased to almost zero in a few seconds). The hydrophilic CNF barrier layer in the TFNC membrane proved to have remarkably high antifouling properties (the fouling ratio <10%) even at extended periods of time (up to 48 $hr$), whereas the conventional membranes exhibited a very high fouling ratio (about 35%). Furthermore, the CNF based TFNC membranes showed a higher protein rejection ratio when compared with the conventional membranes, which could be attributed to the strong electrostatic charge repulsion between the CNF layer surface and the protein molecules (both were negatively charged in water under the neutral conditions). The effects of the CNF barrier layer thickness on the fouling tendency and the permeation flux were also examined. Interestingly, as the barrier layer thickness decreased, the flux increased quite drastically. However, when the CNF layer was too thin, the roughness of the surface layer also increased, which resulted in an increase in fouling.

## Notes

The authors declare no competing financial interests.

## Acknowledgement

This work was supported by a grant to the Center for Clean Water Technology from the New York State Department of Environmental Conservation (DEC01-C00366GG-3350000) and a grant from the National Science Foundation (DMR-1808690). The authors would like to thank the Advanced Energy Research and Technology Center (AERTC) and Central Microscopy Imaging Center (CMIC) for carrying out the SEM and TEM measurements.

## References

[1] Ihsanullah, Carbon nanotube membranes for water purification: developments, challenges, and prospects for the future, Separ. Purif. Technol. 209 (2019) 307–337, https://doi.org/10.1016/j.seppur.2018.07.043.
[2] B.A. Getachew, S.R. Kim, J.H. Kim, Self-healing hydrogel pore-filled water filtration membranes, Environ. Sci. Technol. 51 (2017) 905–913, https://doi.org/10.1021/acs.est.6b04574.
[3] K. Kimura, N. Yamato, H. Yamamura, Y. Watanabe, Membrane fouling in pilot-scale membrane bioreactors (MBRs) treating municipal wastewater, Environ. Sci. Technol. 39 (2005) 6293–6299, https://doi.org/10.1021/es0502425.
[4] P. Cruz-Tato, E.O. Ortiz-Quiles, K. Vega-Figueroa, L. Santiago-Martoral, M. Flynn, L.M. Díaz-Vázquez, E. Nicolau, Metalized nanocellulose composites as a feasible material for membrane supports: design and applications for water treatment, Environ. Sci. Technol. 51 (2017) 4585–4595, https://doi.org/10.1021/acs.est.6b05955.
[5] W. Chen, C. Qian, W.L. Hong, J.X. Cheng, H.Q. Yu, Evolution of membrane fouling revealed by label-free vibrational spectroscopic imaging, Environ. Sci. Technol. 51 (2017) 9580–9587, https://doi.org/10.1021/acs.est.7b02775.
[6] M.C. Barry, K. Hristovski, P. Westerhoff, Membrane fouling by vesicles and prevention through ozonation, Environ. Sci. Technol. 48 (2014) 7349–7356, https://doi.org/10.1021/es500435e.
[7] Y.N. Wang, C.Y. Tang, Fouling of nanofiltration, reverse osmosis, and ultrafiltration membranes by protein mixtures: the role of inter-foulant-species interaction, Environ. Sci. Technol. 45 (2011) 6373–6379, https://doi.org/10.1021/es2013177.
[8] Q. Jiang, D. Ghim, S. Cao, S. Tadepalli, K.-K. Liu, H. Kwon, J. Luan, Y. Min, Y.-S. Jun, S. Singamaneni, Photothermally active reduced graphene oxide/bacterial nanocellulose composites as biofouling-resistant ultrafiltration membranes, Environ. Sci. Technol. 53 (2019) 412–421, https://doi.org/10.1021/acs.est.8b02772.
[9] H.K. Shon, S. Vigneswaran, I.S. Kim, J. Cho, H.H. Ngo, Effect of pretreatment on the fouling of membranes: application in biologically treated sewage effluent, J. Membr. Sci. 234 (2004) 111–120, https://doi.org/10.1016/j.memsci.2004.01.015.
[10] J. Mansouri, S. Harrisson, V. Chen, Strategies for controlling biofouling in membrane filtration systems: challenges and opportunities, J. Mater. Chem. 20 (2010) 4567–4586, https://doi.org/10.1039/b926440j.
[11] D. Wandera, H.H. Himstedt, M. Marroquin, S.R. Wickramasinghe, S.M. Husson, Modification of ultrafiltration membranes with block copolymer nanolayers for produced water treatment: the roles of polymer chain density and polymerization time on performance, J. Membr. Sci. 403–404 (2012) 250–260, https://doi.org/10.1016/j.memsci.2012.02.061.
[12] A. Ouradi, Q.T. Nguyen, A. Benaboura, Polysulfone-AN69 blend membranes and its surface modification by polyelectrolyte-layer deposit-Preparation and characterization, J. Membr. Sci. 454 (2014) 20–35, https://doi.org/10.1016/j.memsci.2013.11.048.
[13] D. Wandera, S.M. Husson, Assessment of fouling-resistant membranes for additive-free treatment of high-strength wastewaters, Desalination 309 (2013) 222–230, https://doi.org/10.1016/j.desal.2012.10.013.
[14] F. Gao, J. Wang, H. Zhang, H. Jia, Z. Cui, G. Yang, Aged PVDF and PSF ultrafiltration membranes restored by functional polydopamine for adjustable pore sizes and fouling control, J. Membr. Sci. 571 (2019) 156–167, https://doi.org/10.1016/j.memsci.2018.10.037.
[15] K.R. Kull, M.L. Steen, E.R. Fisher, Surface modification with nitrogen-containing plasmas to produce hydrophilic, low-fouling membranes, J. Membr. Sci. 246 (2005) 203–215, https://doi.org/10.1016/j.memsci.2004.08.019.
[16] A. Schulze, B. Marquardt, M. Went, A. Prager, M.R. Buchmeiser, Electron beam-based functionalization of polymer membranes, Water Sci. Technol. 65 (2012) 574–580.
[17] J. Ravereau, A. Fabre, A. Brehant, R. Bonnard, C. Sollogoub, J. Verdu, Ageing of polyvinylidene fluoride hollow fiber membranes in sodium hypochlorite solutions, J. Membr. Sci. 505 (2016) 174–184, https://doi.org/10.1016/j.memsci.2015.12.063.
[18] C.N. Wu, T. Saito, Q. Yang, H. Fukuzumi, A. Isogai, Increase in the water contact angle of composite film surfaces caused by the assembly of hydrophilic nanocellulose fibrils and nanoclay platelets, ACS Appl. Mater. Interfaces 6 (2014) 12707–12712, https://doi.org/10.1021/am502701e.
[19] S. Gustafsson, L. Manukyan, A. Mihranyan, Protein-nanocellulose interactions in paper filters for advanced separation applications, Langmuir 33 (2017) 4729–4736, https://doi.org/10.1021/acs.langmuir.7b00566.
[20] C. Aulin, G. Ström, Multilayered alkyd resin/nanocellulose coatings for use in renewable packaging solutions with a high level of moisture resistance, Ind. Eng. Chem. Res. 52 (2013) 2582–2589, https://doi.org/10.1021/ie301785a.
[21] T.S. Anirudhan, S.R. Rejeena, Adsorption and hydrolytic activity of trypsin on a

carboxylate-functionalized cation exchanger prepared from nanocellulose, J. Colloid Interface Sci. 381 (2012) 125–136, https://doi.org/10.1016/j.jcis.2012.05.024.
[22] M. Visanko, H. Liimatainen, J.A. Sirviö, A. Haapala, R. Sliz, J. Niinimäki, O. Hormi, Porous thin film barrier layers from 2,3-dicarboxylic acid cellulose nanofibrils for membrane structures, Carbohydr. Polym. 102 (2014) 584–589, https://doi.org/10.1016/j.carbpol.2013.12.006.
[23] M. Visanko, H. Liimatainen, J.A. Sirviö, O. Hormi, A cross-linked 2,3-dicarboxylic acid cellulose nanofibril network: a nanoporous thin-film layer with tailored pore size for composite membranes, Separ. Purif. Technol. 154 (2015) 44–50, https://doi.org/10.1016/j.seppur.2015.09.026.
[24] K.W. Kolewe, K.M. Dobosz, K.A. Rieger, C.C. Chang, T. Emrick, J.D. Schiffman, Antifouling electrospun nanofiber mats functionalized with polymer zwitterions, ACS Appl. Mater. Interfaces 8 (2016) 27585–27593, https://doi.org/10.1021/acsami.6b09839.
[25] H. Ma, C. Burger, B.S. Hsiao, B. Chu, Fabrication and characterization of cellulose nanofiber based thin-film nanofibrous composite membranes, J. Membr. Sci. 454 (2014) 272–282, https://doi.org/10.1016/j.memsci.2013.11.055.
[26] H. Ma, C. Burger, B.S. Hsiao, B. Chu, Ultrafine polysaccharide nanofibrous membranes for water purification, Biomacromolecules 12 (2011) 970–976, https://doi.org/10.1021/bm1013316.
[27] H. Ma, K. Yoon, L. Rong, Y. Mao, Z. Mo, D. Fang, Z. Hollander, J. Gaiteri, B.S. Hsiao, B. Chu, High-flux thin-film nanofibrous composite ultrafiltration membranes containing cellulose barrier layer, J. Mater. Chem. 20 (2010) 4692–4704, https://doi.org/10.1039/b922536f.
[28] R. Arvidsson, D. Nguyen, M. Svanström, Life cycle assessment of cellulose nanofibrils production by mechanical treatment and two different pretreatment processes, Environ. Sci. Technol. 49 (2015) 6881–6890, https://doi.org/10.1021/acs.est.5b00888.
[29] R. Hiraoki, Y. Ono, T. Saito, A. Isogai, Molecular mass and molecular-mass distribution of TEMPO-oxidized celluloses and TEMPO-oxidized cellulose nanofibrils, Biomacromolecules 16 (2015) 675–681, https://doi.org/10.1021/bm501857c.
[30] A. Isogai, T. Saito, H. Fukuzumi, TEMPO-oxidized cellulose nanofibers, Nanoscale 3 (2011) 71–85, https://doi.org/10.1039/C0NR00583E.
[31] T. Saito, S. Kimura, Y. Nishiyama, A. Isogai, Cellulose nanofibers prepared by TEMPO-mediated oxidation of native cellulose, Biomacromolecules 8 (2007) 2485–2491, https://doi.org/10.1021/bm0703970.
[32] A.C. Corrêa, E.M. de Teixeira, L.A. Pessan, L.H.C. Mattoso, Cellulose nanofibers from curaua fibers, Cellulose 17 (2010) 1183–1192, https://doi.org/10.1007/s10570-010-9453-3.
[33] W. Chen, H. Yu, Y. Liu, P. Chen, M. Zhang, Y. Hai, Individualization of cellulose nanofibers from wood using high-intensity ultrasonication combined with chemical pretreatments, Carbohydr. Polym. 83 (2011) 1804–1811, https://doi.org/10.1016/j.carbpol.2010.10.040.
[34] Y. Mao, K. Liu, C. Zhan, L. Geng, B. Chu, B.S. Hsiao, Characterization of nanocellulose using small-angle neutron, X-ray, and dynamic light scattering techniques, J. Phys. Chem. B 121 (2017) 1340–1351, https://doi.org/10.1021/acs.jpcb.6b11425.
[35] J. Praskalo, M. Kostic, A. Potthast, G. Popov, B. Pejic, P. Skundric, Sorption properties of TEMPO-oxidized natural and man-made cellulose fibers, Carbohydr. Polym. 77 (2009) 791–798, https://doi.org/10.1016/j.carbpol.2009.02.028.
[36] R. Shinoda, T. Saito, Y. Okita, A. Isogai, Relationship between length and degree of polymerization of TEMPO-oxidized cellulose nanofibrils, Biomacromolecules 13 (2012) 842–849, https://doi.org/10.1021/bm2017542.
[37] D. Rana, T. Matsuura, Surface modifications for antifouling membranes, Chem. Rev. 110 (2010) 2448–2471.
[38] M. Zhang, Q.T. Nguyen, Z. Ping, Hydrophilic modification of poly (vinylidene fluoride) microporous membrane, J. Membr. Sci. 327 (2009) 78–86, https://doi.org/10.1016/j.memsci.2008.11.020.
[39] H. Fan, K. Xiao, S. Mu, Y. Zhou, J. Ma, X. Wang, X. Huang, Impact of membrane pore morphology on multi-cycle fouling and cleaning of hydrophobic and hydrophilic membranes during MBR operation, J. Membr. Sci. 556 (2018) 312–320, https://doi.org/10.1016/j.memsci.2018.04.014.
[40] A. Mautner, K.Y. Lee, T. Tammelin, A.P. Mathew, A.J. Nedoma, K. Li, A. Bismarck, Cellulose nanopapers as tight aqueous ultra-filtration membranes, React. Funct. Polym. 86 (2015) 209–214, https://doi.org/10.1016/j.reactfunctpolym.2014.09.014.
[41] W. Fu, L. Hua, W. Zhang, Experimental and modeling assessment of the roles of hydrophobicity and zeta potential in chemically modified poly(ether sulfone) membrane fouling kinetics, Ind. Eng. Chem. Res. 56 (2017) 8580–8589, https://doi.org/10.1021/acs.iecr.7b02203.
[42] J. Arkani-Hamed, The lunar mascons revisited, J. Geophys. Res. E Planets 103 (1998) 3709–3739, https://doi.org/10.1021/acsami.7b02382.
[43] K. Xiao, X. Wang, X. Huang, T.D. Waite, X. Wen, Combined effect of membrane and foulant hydrophobicity and surface charge on adsorptive fouling during microfiltration, J. Membr. Sci. 373 (2011) 140–151, https://doi.org/10.1016/j.memsci.2011.02.041.
[44] M. Elimelech, X. Zhu, A.E. Childress, S. Hong, Role of membrane surface morphology in colloidal fouling of cellulose acetate and composite aromatic polyamide reverse osmosis membranes, J. Mater. Sci. 127 (1997) 101–109.
[45] E.M.V. Hoek, S. Bhattacharjee, M. Elimelech, Effect of membrane surface roughness on colloid-membrane DLVO interactions, Langmuir 19 (2003) 4836–4847, https://doi.org/10.1021/la027083c.
[46] Y.N. Wang, C.Y. Tang, Nanofiltration membrane fouling by oppositely charged macromolecules: investigation on flux behavior, foulant mass deposition, and solute rejection, Environ. Sci. Technol. 45 (2011) 8941–8947, https://doi.org/10.1021/es202709r.
[47] K. Xiao, Y. xiao Shen, S. Liang, P. Liang, X. mao Wang, X. Huang, A systematic analysis of fouling evolution and irreversibility behaviors of MBR supernatant hydrophilic/hydrophobic fractions during microfiltration, J. Membr. Sci. 467 (2014) 206–216, https://doi.org/10.1016/j.memsci.2014.05.030.
[48] N. Lin, C. Bruzzese, A. Dufresne, TEMPO-oxidized nanocellulose participating as crosslinking aid for alginate-based sponges, ACS Appl. Mater. Interfaces 4 (2012) 4948–4959, https://doi.org/10.1021/am301325r.